

A robust VEM-based approach for flow simulations in poro-fractured media

Original

A robust VEM-based approach for flow simulations in poro-fractured media / Berrone, S.; Borio, A.; D'Auria, A.; Scialo, S.; Vicini, F.. - In: MATHEMATICAL MODELS AND METHODS IN APPLIED SCIENCES. - ISSN 0218-2025. - ELETTRONICO. - (2021), pp. 1-31. [10.1142/S0218202521500639]

Availability:

This version is available at: 11583/2949154 since: 2022-01-14T11:43:54Z

Publisher:

World Scientific

Published

DOI:10.1142/S0218202521500639

Terms of use:

This article is made available under terms and conditions as specified in the corresponding bibliographic description in the repository

Publisher copyright

(Article begins on next page)

Mathematical Models and Methods in Applied Sciences
 © World Scientific Publishing Company

A robust VEM based approach for flow simulations in poro-fractured media*

Stefano Berrone[†]

*Politecnico di Torino, Dipartimento di Scienze Matematiche
 c.so Duca Degli Abruzzi, 24, 10122, Torino, Italy
 stefano.berrone@polito.it*

Andrea Borio

*Politecnico di Torino, Dipartimento di Scienze Matematiche
 c.so Duca Degli Abruzzi, 24, 10122, Torino, Italy
 andrea.borio@polito.it*

Alessandro D'Auria

*Politecnico di Torino, Dipartimento di Scienze Matematiche
 c.so Duca Degli Abruzzi, 24, 10122, Torino, Italy
 alessandro.dauria@polito.it*

Stefano Scialò

*Politecnico di Torino, Dipartimento di Scienze Matematiche
 c.so Duca Degli Abruzzi, 24, 10122, Torino, Italy
 stefano.scialo@polito.it*

Fabio Vicini

*Politecnico di Torino, Dipartimento di Scienze Matematiche
 c.so Duca Degli Abruzzi, 24, 10122, Torino, Italy
 fabio.vicini@polito.it*

Received (Day Month Year)

Revised (Day Month Year)

Communicated by (xxxxxxxxxx)

A Virtual Element Method (VEM) based approach is proposed for the simulation of flow in fractured porous media. The method is based on a robust meshing strategy, capable of producing conforming polyhedral meshes of intricate geometries and relies on the robustness of the VEM in handling distorted and elongated elements. Numerical tests in challenging configurations are presented and discussed, also in a time-dependent setting to show the viability and the effectiveness of the method.

Keywords: VEM; Complex Geometries; DFM; Geological Problems, 2D-3D Flow Cou-

* Authors are members of INdAM research group GNCS

[†]corresponding author

2 *Berrone, Borio, D'Auria, Scialò, Vicini*

pling; 2D-3D Conforming Meshes.

AMS Subject Classification: 65N30, 65N50

1. Introduction

Despite the recent advancements in terms of availability of computational resources, the effective simulation of underground phenomena is still a challenging task, thus stimulating the research for the development of innovative numerical schema. Difficulties mainly arise from the geometrical complexity of the involved computational domains, aggravated by the uncertain nature of input data on the subsoil, which demand for repeated simulations to derive reliable statistics on the selected quantities of interest.^{25,47}

In the present work we consider the computation of the hydraulic head in a fractured porous medium, described by means of the Discrete Fracture and Matrix^{2,4,5,21,23,30,49} (DFM) model. Fractures are thin regions in the domain characterized by geological properties different from those of the surrounding medium. When the domain size is much larger than the fracture thickness, simplified models are introduced to represent the fractures at an affordable computational cost. In DFM models (DFMs) fractures are dimensionally reduced to planar objects in the three dimensional space and some coupling conditions are introduced to close the problem at fracture-fracture intersections, often called traces, and at fracture-matrix interfaces.⁴⁰ Fractures are randomly generated according to probability distributions on their position, orientation, density and hydraulic properties. DFM models constitute an alternative to homogenization techniques,⁴⁸ dual and multiporosity models,²⁷ or Embedded Discrete Fracture Matrix (EDFM) models;^{39,41} DFMs have the advantageous characteristic of providing an explicit representation of the underground fracture network, which might be critical for applications where flow directionality and characteristic flow paths might play a relevant role, as for geothermal applications, geological waste storage, water resources monitoring, or in Oil&Gas enhanced production. On the other hand, due to the random nature of the data, DFM models still present complex and multi-scale geometries, now due to the presence of fractures forming narrow angles and forming intersections which span several orders of magnitude. A partially simplified problem can be obtained by neglecting the porous matrix in the simulations, which can provide acceptable results when the matrix has a permeability much lower than the fractures; this originates the so-called Discrete Fracture Network model (DFN),^{29,31,42,46} which however still present the complexities related to the presence of a randomly generated fractures. Anyway, in both DFM and DFN simulations, robust and efficient numerical tools to handle severe geometrical configurations, are of paramount importance.

In standard approximation techniques the imposition of interface conditions for DFM/DFN simulations requires the use of a mesh conforming to the interfaces; on the other hand, the use of non conforming meshes requires unconventional numerical schema for the treatment of non-conformities.³⁴ Effective conforming meshing

strategies can be used with standard finite element or finite volume schema,^{38,43,50} or the problem can be reduced to the interfaces^{44,45} by removing the unknowns in the interior of the fractures. Non conforming meshes can be handled instead by introducing XFEM based approximations^{32,35} or through unconventional domain decomposition schemes.^{18–22} Methods based on polytopal meshes are recently gaining increasing popularity for DFM/DFN simulations, given the possibility of an easier generation of conforming meshes using elements with general polygonal/polyhedral shapes. There are several examples of such polytopal methods for instance Mimetic Finite Difference (MFD) method,^{3,5} Hybrid High Order (HHO) methods²⁶ and Virtual Element Methods (VEM).^{10–14,17,28,33,36}

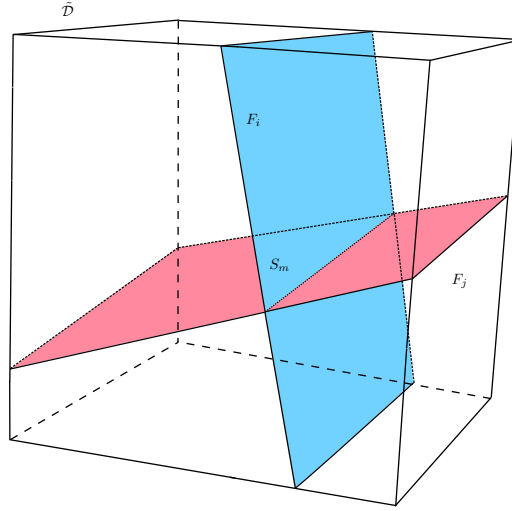
In the present work a time-dependent Darcy law is solved in complex DFM models by means of the Virtual Element Method (VEM).^{1,7–9} Continuity of the hydraulic head and flux balance is assumed at fracture-fracture intersections and fracture-matrix interfaces. Exploiting the robustness of the VEM in handling distorted elements,¹⁶ a conforming mesh is built splitting an original regular non-conforming mesh into a mesh not crossing the interfaces. This is achieved through an efficient meshing strategy which builds a tree of each mesh cell, where children cells are originated by the parent cell by a cut processes of the cell itself or of part of its boundary. After the discretization, a problem with symmetric positive definite matrix needs to be solved at each time-step thus allowing to efficiently solve extremely complex configurations. This meshing strategy is here proposed for the first time for DFM simulations in conjunction with a primal formulation of the problem and for time-dependent simulations. Further, the present work deals with realistic problems where the use of polytopal methods is fundamental, since polytopal meshes naturally arise from the domain itself. For this reason a mesh generation process tailored to the specific problem is presented and discussed.

The paper is organized as follows: Section 2 describes the continuous non-stationary problem on the porous matrix and the fracture network; Section 3 and Section 4 are devoted to introduce the conforming mesh approach and the VEM discretization space used on the numerical results proposed in Section 5.

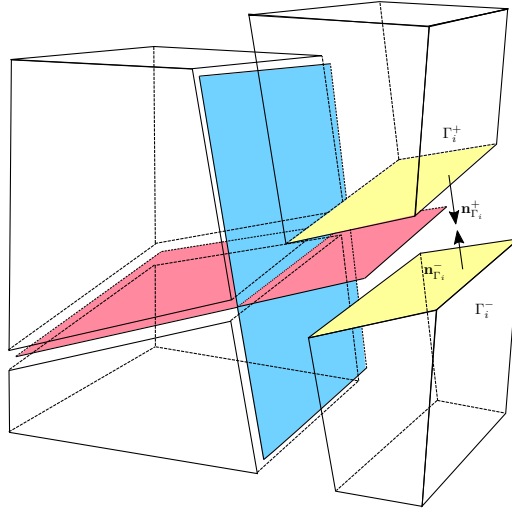
2. Problem description

Let us now formulate the DFM problem to be solved in a polyhedral block of porous material, denoted as \mathcal{D} with boundary $\partial\mathcal{D}$, crossed by a fracture network Ω , as the one shown in Figure 1. The network Ω is given by the union of convex planar polygons F_i representing the fractures immersed in the porous medium, i.e., $\Omega \subset \mathcal{D} = \bigcup_{i=1}^{N_F} F_i$. The boundary of Ω is given by the union of the boundaries of the single fractures: $\partial\Omega = \bigcup_{i=1}^{N_F} \partial F_i$. Fractures might intersect forming segments, or traces, here denoted by S_m , for $m = 1, \dots, N_S$. For simplicity of exposition, we assume that each trace is given by the intersection of exactly two fractures, such that an injective map $\sigma : [1, N_S] \mapsto [1, N_F] \times [1, N_F]$ can be defined between a trace index and a couple of fracture indexes $\sigma(m) = \{i, j\}$ being $S_m = \bar{F}_i \cap \bar{F}_j$.

4 Berrone, Borio, D'Auria, Scialò, Vicini



(a) \mathcal{D} and Ω



(b) Γ_i^\pm and $\underline{n}_{\Gamma_i^\pm}$

Fig. 1: Example DFM and nomenclature

The boundary $\partial\mathcal{D}$ is split in a Dirichlet part Γ_D , with $|\Gamma_D| \neq 0$ and a Neumann part Γ_N , with $\Gamma_D \cap \Gamma_N = \emptyset$, where Dirichlet and Neumann boundary conditions are prescribed, respectively. The same boundary conditions apply to the portions of the fracture network boundary that intersects Γ_D and Γ_N , whereas internal boundaries of Ω , i.e., such that $|\partial\Omega \cap \partial\mathcal{D}| = 0$, are considered as no-flow boundaries.

We will denote by $\tilde{\mathcal{D}} = \mathcal{D} \setminus \bar{\Omega}$ the original block \mathcal{D} without the internal fractures

and, similarly, by \tilde{F}_i each fracture without the intersection segments with other fractures. Fractures coincide with portions of the boundary of the domain $\tilde{\mathcal{D}}$, and we call Γ_i^\pm the two sides of the boundary of $\tilde{\mathcal{D}}$ around F_i , see Figure 1. The outward pointing unit normal vector to Γ_i^\pm is $\underline{n}_{\Gamma_i^\pm}$ and a jump operator

$$[\![\underline{v} \cdot \underline{n}]\!]_{\Gamma_i} := \left(\underline{v}|_{\Gamma_i^+} \cdot \underline{n}_{\Gamma_i^+} \right) - \left(\underline{v}|_{\Gamma_i^-} \cdot \underline{n}_{\Gamma_i^-} \right)$$

is defined across Γ_i for sufficiently regular vector functions \underline{v} in $\tilde{\mathcal{D}}$. Similarly, having $\underline{n}_{S_m}^i$ the outward unit normal vector to S_m on the fracture F_i plane,

$$[\![\underline{w}_i \cdot \underline{n}]\!]_{S_m} := \left(\underline{w}_i|_{S_m^+} \cdot \underline{n}_{S_m}^i \right) - \left(\underline{w}_i|_{S_m^-} \cdot \underline{n}_{S_m}^i \right)$$

is the jump operator across the two sides S_m^\pm of the portion of the boundary of \tilde{F}_i for sufficiently regular functions \underline{w}_i defined on \tilde{F}_i . The hydraulic transmissivity in $\tilde{\mathcal{D}}$ is the uniformly positive definite tensor $\underline{K}_{\tilde{\mathcal{D}}} : \mathbb{R}^3 \rightarrow \mathbb{R}^{3 \times 3}$, whereas the uniformly positive definite tensor $\underline{K}_i : \mathbb{R}^2 \rightarrow \mathbb{R}^{2 \times 2}$ denotes the in-plane fracture transmissivity. Finally, ∇ represents the three-dimensional gradient in $\tilde{\mathcal{D}}$ whereas ∇_i is the tangential gradient on the plane of fracture F_i . The problem of the unsteady distribution of the hydraulic head H in \mathcal{D} can be then stated in strong formulation as:

$$\frac{\partial H_{\mathcal{D}}}{\partial t} - \nabla \cdot \left(\underline{K}_{\tilde{\mathcal{D}}} \nabla H_{\mathcal{D}} \right) = s \quad \text{in } \tilde{\mathcal{D}} \times (0, T] \quad (2.1)$$

$$\frac{\partial H_i}{\partial t} - \nabla_i \cdot \left(\underline{K}_i \nabla_i H_i \right) = -[\![\underline{K}_{\tilde{\mathcal{D}}} \nabla H_{\mathcal{D}} \cdot \underline{n}]\!]_{\Gamma_i} \quad \text{in } \tilde{F}_i \times (0, T], \quad i \in [1, N_F] \quad (2.2)$$

$$(H_{\mathcal{D}})|_{\Gamma_i^\pm} = H_i, \quad i \in [1, N_F] \quad (2.3)$$

$$H_i|_{S_m} = H_j|_{S_m}, \quad m \in [1, N_S], \quad \{i, j\} = \sigma(m) \quad (2.4)$$

$$[\![\underline{K}_i \nabla_i H_i \cdot \underline{n}]\!]_{S_m} = -[\![\underline{K}_j \nabla_j H_j \cdot \underline{n}]\!]_{S_m}, \quad m \in [1, N_S], \quad \{i, j\} = \sigma(m) \quad (2.5)$$

$$H = H^0 \quad \text{in } \mathcal{D}, \quad t = 0 \quad (2.6)$$

$$H = 0 \quad \text{on } \Gamma_D \times (0, T] \quad (2.7)$$

$$\underline{K}_{\tilde{\mathcal{D}}} \nabla H \cdot \underline{n}_{\Gamma_N} = 0 \quad \text{on } \Gamma_N \times (0, T] \quad (2.8)$$

where $H_{\mathcal{D}}$ is the restriction of the hydraulic head to $\tilde{\mathcal{D}}$ and H_i the hydraulic head on F_i , $i = 1, \dots, N_F$; s is a volumetric source term and time t ranges in the interval $(0, T]$, $T > 0$ with $H = H^0$ the initial condition. For simplicity, homogeneous Dirichlet and Neumann boundary conditions are used, the extension to the more general case being immediate.

Let us now derive the weak formulation of problem (2.1)-(2.8). We will denote by $(\cdot, \cdot)_\Omega$ the L^2 -scalar product in Ω and by $(\cdot, \cdot)_{F_i}$ the counterpart on F_i and assume $\underline{K}_{\tilde{\mathcal{D}}} \in L^\infty(\mathcal{D})$, $\underline{K}_i \in L^\infty(F_i)$, $\forall i \in \{1, \dots, N_F\}$. To this end we introduce the function space $V(\mathcal{D})$:

$$V(\mathcal{D}) = \{v \in H_0^1(\mathcal{D}) : v_i := \text{tr}_{F_i} v \in H_{0, \Gamma_D}^1(F_i), \quad \forall i = 1, \dots, N_F, \\ \text{tr}_{S_m} v_i = \text{tr}_{S_m} v_j, \quad \forall m = 1, \dots, N_S, i, j = \sigma(m)\}$$

thus containing functions in H_0^1 of the whole domain \mathcal{D} whose trace on each fracture is a function in $H_{0,\Gamma_D}^1(F_i) \forall i = 1, \dots, N_F$, which represents the subspace of $H^1(F_i)$ of functions having zero trace on $\partial F_i \cap \Gamma_D$. Consequently, functions in $V(\mathcal{D})$ satisfy the coupling conditions (2.3), (2.4) and (2.5) at the interfaces. We then introduce the space:

$$\mathcal{V} = \left\{ v \in V(\mathcal{D}) : \int_0^T \|v\|_V^2 < \infty \text{ and } \int_0^T \left\| \frac{\partial v}{\partial t} \right\|_{V'}^2 < \infty \right\}.$$

The weak formulation of the problem at hand thus reads: find $H \in \mathcal{V}$ such that, for all $v \in V(\mathcal{D})$

$$\left(\frac{\partial H}{\partial t}, v \right)_{\mathcal{D}} + \sum_{i=1}^{N_F} \left(\frac{\partial H_i}{\partial t}, v_i \right)_{F_i} + \left(\underline{K}_{\mathcal{D}} \nabla H, \nabla v \right)_{\mathcal{D}} + \sum_{i=1}^{N_F} \left(\underline{K}_i \nabla_i H_i, \nabla_i v_i \right)_{F_i} = (s, v)_{\mathcal{D}}. \quad (2.9)$$

By classical arguments, it can be shown that problem (2.9) is well posed, since $V(\mathcal{D})$ is a Hilbert space with the scalar product:^{21, 23}

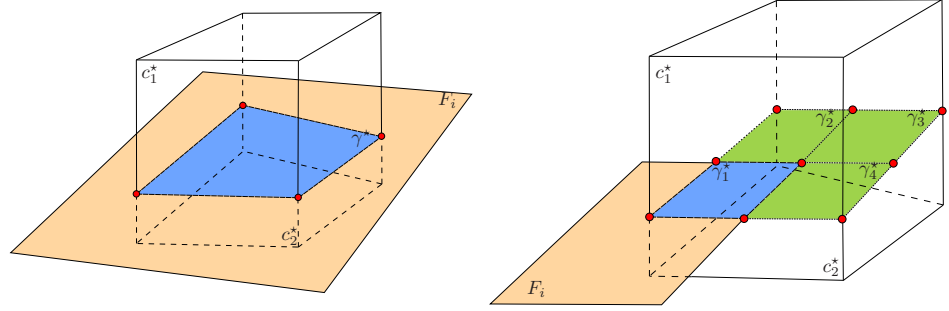
$$a(v, w) := \left(\underline{K}_{\mathcal{D}} \nabla v, \nabla w \right)_{\mathcal{D}} + \sum_{i=1}^{N_F} \left(\underline{K}_i \nabla_i w_i, \nabla_i v_i \right)_{F_i}. \quad (2.10)$$

3. Domain discretization

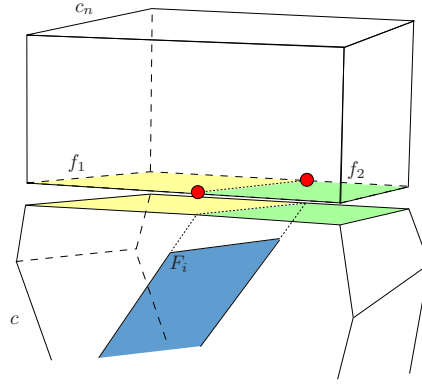
We now describe how to build a global conforming mesh $\mathcal{T}_{\mathcal{D}}$ on the DFM domain \mathcal{D} . Introducing the notation used in the following, given a generic mesh $\mathcal{T} = \{\mathcal{C}_{\mathcal{T}}, \mathcal{F}_{\mathcal{T}}, \mathcal{E}_{\mathcal{T}}, \mathcal{V}_{\mathcal{T}}\}$, $\mathcal{C}_{\mathcal{T}}$ denotes the set of the mesh elements, $\mathcal{F}_{\mathcal{T}}$ is the set of the faces forming the boundaries of mesh cells, $\mathcal{E}_{\mathcal{T}}$ is the set of face boundary edges and $\mathcal{V}_{\mathcal{T}}$ collects all the mesh vertices. The first step to build $\mathcal{T}_{\mathcal{D}}$ consists in the generation of a mesh of the closure of domain \mathcal{D} made of simple elements, such as cubes or tetrahedra, independently of the embedded fracture network, see for example Figure 6. Let us denote this initial mesh as $\mathcal{T}_{\delta}^0 = \{\mathcal{C}_{\mathcal{T}_{\delta}}^0, \mathcal{F}_{\mathcal{T}_{\delta}}^0, \mathcal{E}_{\mathcal{T}_{\delta}}^0, \mathcal{V}_{\mathcal{T}_{\delta}}^0\}$, where $\delta \in \mathbb{R}$ is the mesh parameter used to control the size of the elements of the mesh, as for example the maximum diameter of the cells. This initial mesh will be then cut with N_F steps into a mesh $\mathcal{T}_{\delta}^{N_F} = \{\mathcal{C}_{\mathcal{T}_{\delta}}^{N_F}, \mathcal{F}_{\mathcal{T}_{\delta}}^{N_F}, \mathcal{E}_{\mathcal{T}_{\delta}}^{N_F}, \mathcal{V}_{\mathcal{T}_{\delta}}^{N_F}\}$ made of general polyhedra conforming to the interfaces.

Cell Identification

According to the arbitrary ordering of the fractures in the network Ω , let us first consider fracture F_1 and let us call π_{F_1} the plane on which F_1 lies. Let further $\mathcal{F}_{\mathcal{T}_{\delta}, F_1} \subset \mathcal{F}_{\mathcal{T}_{\delta}}^0$ be the set of faces f^* having an intersection with F_1 of non-vanishing measure, i.e., $\mathcal{F}_{\mathcal{T}_{\delta}, F_1} = \{f^* \in \mathcal{F}_{\mathcal{T}_{\delta}}^0 : |f^* \cap F_1| > 0\}$, for example the four lateral faces of the cell in Figure 2a or the front and right face of cell in Figure 2b. A set of mesh cells $\mathcal{C}_{\mathcal{T}_{\delta}, F_1} \subset \mathcal{C}_{\mathcal{T}_{\delta}}^0$ is then created, containing all the cells having at least one boundary face belonging to $\mathcal{F}_{\mathcal{T}_{\delta}, F_1}$.



(a) Mesh cell cut along a fracture plane with $\gamma^* \subset F_i$ (b) Mesh cell cut along a fracture plane with $\gamma^* \not\subset F_i$, and subsequent splitting of γ^*



(c) Mesh elements c_n neighboring cut cells c are updated with the references to the newly generated mesh objects.

Fig. 2: Mesh generation process

Cutting

Subsequently, each cell $c^* \in \mathcal{C}_{\mathcal{T}_\delta, F_1}$ is split along the fracture plane π_{F_1} into two sub-cells c_1^* and c_2^* (see Figure 2a). New edges and new vertices are created accordingly. Please note that, in case the fracture F_1 does not entirely cross the cell c^* , the common face of c_1^* and c_2^* , $\gamma^* = c_1^* \cap c_2^* = c^* \cap \pi_{F_1}$ may be only partially inside fracture F_1 (see Figure 2b). In case the cell c^* has a face on the plane π_{F_1} , either c_1^* or c_2^* might be a degenerate polyhedron. The degenerate polyhedron is discarded.

8 *Berrone, Borio, D'Auria, Scialò, Vicini*

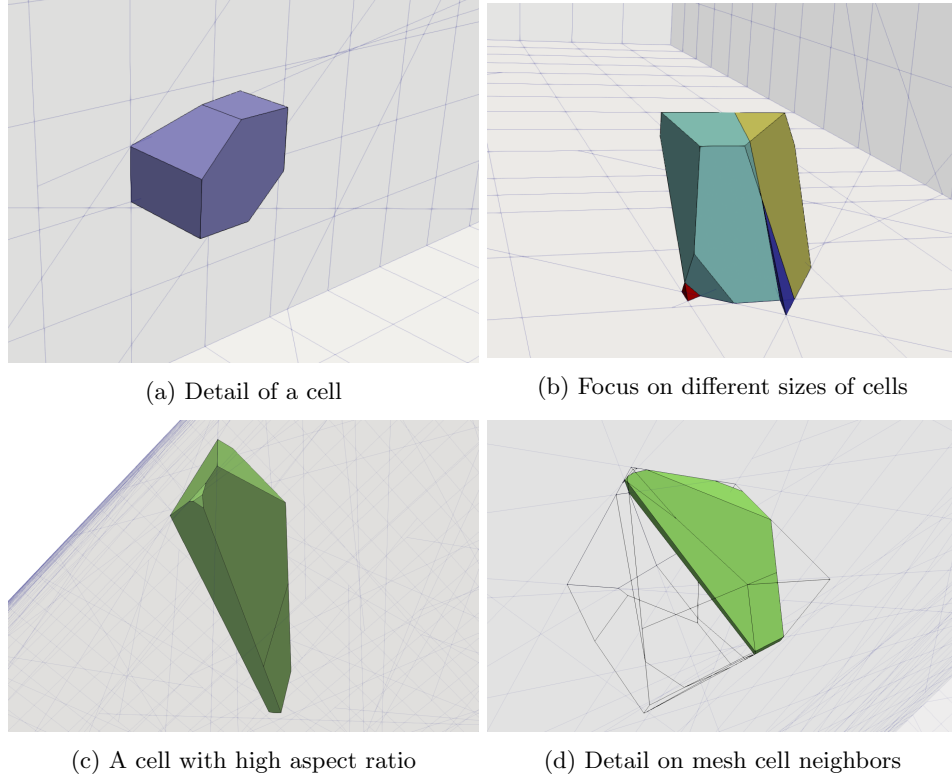


Fig. 3: Example of 3D VEM cells

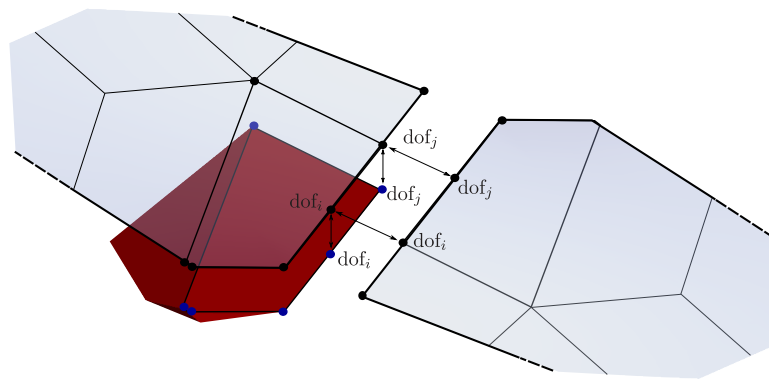


Fig. 4: Choice of degrees of freedom to enforce solution continuity at the interfaces

Mesh update

The newly generated cells, faces and edges produced by the cut are inserted in the mesh \mathcal{T}_δ^1 . When a face or an edge of a cell is replaced by two new faces or edges

in the cutting phase, the corresponding changes also affect the neighbouring cells, along with the newly generated vertices, see Figure 2c.

Mesh conforming

The intersection $\gamma^* = c_1^* \cap c_2^*$ is added to a set \mathcal{G}_{F_1} , such that, after all the cells in $\mathcal{C}_{\mathcal{T}_\delta, F_1}$ are processed, \mathcal{G}_{F_1} contains a set of polygons all lying on plane π_{F_1} ; some of these polygons might be partially outside the fracture, see Figure 2b. Polygons in \mathcal{G}_{F_1} completely internal to fracture F_1 already belong to the set $\mathcal{F}_{\mathcal{T}_\delta}^1$, along with the newly generated edges and vertices in $\mathcal{E}_{\mathcal{T}_\delta}^1$ and $\mathcal{V}_{\mathcal{T}_\delta}^1$, respectively. Then each face $\gamma^* \in \mathcal{G}_{F_1}$ partially outside F_1 is split into p convex sub-polygons, such that $\gamma_1^* \equiv \gamma^* \cap F_1$ and $\gamma^* = \bigcup_{\zeta=1}^p \gamma_\zeta^*$ (Figure 2b). The polygon γ^* and its edges are removed from \mathcal{T}_δ^1 and polygons γ_ζ^* , $\zeta = 1, \dots, p$ and the newly generated edges and vertices are added to $\mathcal{F}_{\mathcal{T}_\delta}^1$, $\mathcal{E}_{\mathcal{T}_\delta}^1$ and $\mathcal{V}_{\mathcal{T}_\delta}^1$, respectively, resulting in the final mesh \mathcal{T}_δ^1 .

The process described to produce \mathcal{T}_δ^1 from \mathcal{T}_δ^0 is then repeated for all the fractures F_i , with $i \in [2, N_F]$ obtaining $\mathcal{T}_\delta^{N_F} = \mathcal{T}_\mathcal{D}$ at the end of N_F steps. We denote by $\mathcal{T}_{F_i} \subset \mathcal{F}_{\mathcal{T}_\delta}^{N_F}$ the set of faces f such that $f \subseteq F_i$.

In Figure 3 we show four examples of 3D VEM cells of a mesh $\mathcal{T}_\mathcal{D}$ generated with the algorithm described above; in particular, from Figure 3b and Figure 3d we can appreciate the complexities in the geometry of the cells and the different sizes of neighboring cells which can be produced. Quantitative examples on mesh characteristics are provided in the presentation of the numerical examples of Section 5

Remark 3.1. To optimize memory consumption in the cutting process, each mesh is represented as a forest, being each original element in \mathcal{T} the root of a tree. Each time a polyhedron is cut, it produces two leaves of the tree and each time it is modified, for example by splitting one of its faces, it produces one leaf. Clearly, if a polyhedron is not modified during the process, it is itself considered as a leaf. This way, given a intermediate mesh \mathcal{T}_δ^n of the recursive algorithm, the mesh \mathcal{T}_δ^{n+1} is the mesh obtained collecting all the leaves that are found after applying the above procedure. Furthermore, notice that once the algorithm is applied to \mathcal{T}_δ^n , all the geometric objects that are not leaves of the tree are no more necessary and thus can be safely removed.

Remark 3.2. We note that the description provided in this section is not totally conforming to the implementation that, for efficiency reasons, is slightly more involved introducing a more precise classification of the intersections with the fracture that is used reduce the number of operations on the data structures.

Remark 3.3. In order to reduce the computational cost to build the set $\mathcal{F}_{\mathcal{T}_\delta, F_i}^n = \{f^* \in \mathcal{F}_{\mathcal{T}_\delta}^n : |f^* \cap F_i| > 0\}$ we generate a starting simplicial mesh with informations of the neighborhood. With these information we do not need to build all the set $\mathcal{F}_{\mathcal{T}_\delta, F_i}^n$, but we need only to find one face $f \in \mathcal{F}_{\mathcal{T}_\delta}^n$ for which is true $|f^* \cap F_i| > 0$ and then we find the other ones moving in the neighbourhood of the intersected cells.

4. Problem discretization

Here the discrete version of (2.9) is derived, based on a lowest order conforming Virtual Element Method approximation in primal form.

Let \mathcal{T}_D be a conforming mesh defined as described in Section 3 and let $c \in \mathcal{T}_D$ be a polyhedron and $f \in \mathcal{F}_c$ one of its faces. We denote by $\widehat{\mathbb{P}}_1(f)$ the space of polynomials of degree 1 with respect to the reference system tangential to f , and we introduce the linear projection operator $\Pi_1^{\nabla, f}: H^1(f) \rightarrow \widehat{\mathbb{P}}_1(f)$, defined such that, $\forall v \in H^1(f)$:⁷

$$\begin{cases} \left(\nabla \Pi_1^{\nabla, f} v, \nabla p \right)_f = (\nabla v, \nabla p)_f & \forall p \in \widehat{\mathbb{P}}_1(f), \\ \int_{\partial f} \Pi_1^{\nabla, f} v = \int_{\partial f} v. \end{cases} \quad (4.1)$$

The local VEM space on f is defined, following Ref. 7, using the so called “enhancement” property, as follows:

$$\mathcal{V}_\delta^f = \left\{ v \in H^1(f): \Delta v \in \widehat{\mathbb{P}}_1(f), v \in C^0(\partial f), \text{tr}_{\partial f} v \in \widehat{\mathbb{P}}_1(e) \forall e \in \mathcal{E}_f, \right. \\ \left. (v, p)_f = \left(\Pi_1^{\nabla, f} v, p \right)_f \quad \forall p \in \widehat{\mathbb{P}}_1(f) \right\}, \quad (4.2)$$

where $\widehat{\mathbb{P}}_1(e)$ denotes the spaces of polynomials of degree 1 on each edge e in the set of face boundary edges \mathcal{E}_f , and differential operators are defined with respect to a reference system tangential to f . The scalar product of functions in \mathcal{V}_δ^f against polynomials in $\widehat{\mathbb{P}}_1(f)$ can be computed by means of the projection $\Pi_1^{\nabla, f}$ and definition (4.2). In turn, the computation of $\Pi_1^{\nabla, f} v$ can be performed knowing the analytical expression of v only on the boundary of f , using definition (4.1) and the Gauss-Green formula. Also, the $L^2(f)$ -projection of the gradient of a function in \mathcal{V}_δ^f , $\Pi_0^{0, f} \nabla: \mathcal{V}_\delta^f \rightarrow [\widehat{\mathbb{P}}_0(f)]^2$ can be readily computed starting from the values of v on the boundary of f , since $\nabla \cdot \underline{q} = 0 \forall \underline{q} \in [\widehat{\mathbb{P}}_0(f)]^2$, and then, applying Gauss-Green formula, we get:

$$\forall v \in \mathcal{V}_\delta^f, \quad \left(\Pi_0^{0, f} \nabla v, \underline{q} \right) = \frac{1}{|f|} \int_f \nabla v \cdot \underline{q} = \frac{1}{|f|} \int_{\partial f} v (\underline{q} \cdot \underline{n}), \quad \forall \underline{q} \in [\widehat{\mathbb{P}}_0(f)]^2. \quad (4.3)$$

Similarly, let $\mathbb{P}_1(c)$ be the set of polynomials of degree 1 on a polyhedron $c \in \mathcal{T}_D$ and let $\Pi_1^{\nabla, c}: H^1(c) \rightarrow \mathbb{P}_1(c)$ be the polynomial projection operator such that $\forall v \in H^1(c)$

$$\begin{cases} \left(\nabla \Pi_1^{\nabla, c} v, \nabla p \right)_c = (\nabla v, \nabla p)_c & \forall p \in \mathbb{P}_1(c), \\ \int_{\partial c} \Pi_1^{\nabla, c} v = \int_{\partial c} v. \end{cases} \quad (4.4)$$

We define the following local VEM space on c using again an “enhancement” property:

$$\mathcal{V}_\delta^c = \left\{ v \in H^1(c): \Delta v \in \mathbb{P}_1(c), \text{tr}_f v \in \mathcal{V}_\delta^f \quad \forall f \in \mathcal{F}_c \right. \\ \left. (v, p)_c = \left(\Pi_1^{\nabla, c} v, p \right)_c \quad \forall p \in \mathbb{P}_1(c) \right\}. \quad (4.5)$$

To compute the $\Pi_1^{\nabla, c}$ projection of a function $v \in \mathcal{V}_\delta^c$ we can use definition (4.4) and apply the Gauss-Green formula, thus resulting in the computation of an integral on the boundary of c . Since $\text{tr}_f v \in \mathcal{V}_\delta^f \quad \forall f \in \mathcal{F}_c, \forall v \in \mathcal{V}_\delta^c$, the boundary integral can be computed through the knowledge of v on the boundary of each face of c (see Ref. 6 for details).

The above considerations imply that all projections are computable knowing only the analytical expression of basis functions on the mesh skeleton. Thus, we can choose as degrees of freedom on \mathcal{V}_δ^c the values of a function at the vertices of c , knowing that each VEM function is a linear polynomial on each edge.

Moreover, we define the $L^2(c)$ -orthogonal constant projection of the gradient of a function $v \in \mathcal{V}_\delta^c$, denoted by $\Pi_0^{0, c} \nabla: \mathcal{V}_\delta^c \rightarrow [\mathbb{P}_0(c)]^2$, such that

$$\forall v \in \mathcal{V}_\delta^c, \quad \Pi_0^{0, c} \nabla v = \frac{1}{|c|} \int_c \nabla v. \quad (4.6)$$

This projection is computable resorting, once again, to the Gauss-Green formula and performing integrals of basis functions on faces. Finally, exploiting the last property in (4.5), we can also compute the $L^2(c)$ -projection of VEM functions onto constants, $\Pi_0^{0, c}: \mathcal{V}_\delta^c \rightarrow \mathbb{P}_0(c)$, such that

$$\forall v \in \mathcal{V}_\delta^c, \quad \Pi_0^{0, c} v = \frac{1}{|c|} \int_c v. \quad (4.7)$$

For each $c \in \mathcal{T}_\mathcal{D}$, let $a_\delta^c: \mathcal{V}_\delta^c \times \mathcal{V}_\delta^c \rightarrow \mathbb{R}$ be the bilinear form defined as

$$\forall u, v \in \mathcal{V}_\delta^c, \quad a_\delta^c(u, v) = \left(\underline{K}_\mathcal{D} \Pi_0^{0, c} \nabla u, \Pi_0^{0, c} \nabla v \right)_c + S^c \left(u - \Pi_1^{\nabla, c} u, v - \Pi_1^{\nabla, c} v \right), \quad (4.8)$$

where S^c is a bilinear form defined in such a way that

$$\exists \alpha, \beta > 0: \forall u \in \mathcal{V}_\delta^c, \quad \alpha \left(\underline{K}_\mathcal{D} \nabla u, \nabla u \right)_c \leq a_\delta^c(u, u) \leq \beta \left(\underline{K}_\mathcal{D} \nabla u, \nabla u \right)_c. \quad (4.9)$$

A typical choice for S^c is

$$\forall u, v \in \mathcal{V}_\delta^c, \quad S^c(u, v) = \varrho_c \left\| \underline{K}_\mathcal{D} \right\|_{L^\infty(c)} \sum_{i=1}^{\#\mathcal{V}_\delta^c} \text{dof}_i^c(u) \text{dof}_i^c(v). \quad (4.10)$$

denoting by $\text{dof}_i^c(\cdot)$ the operator selecting the i -th degree of freedom of \mathcal{V}_δ^c and by ϱ_c the cell diameter.

Similarly, for each face f lying on a fracture F_i , we define $a_\delta^f: \mathcal{V}_\delta^f \times \mathcal{V}_\delta^f \rightarrow \mathbb{R}$ such that

$$\forall u, v \in \mathcal{V}_\delta^f, \quad a_\delta^f(u, v) = \left(\underline{K}_i \Pi_0^{0, f} \nabla u, \Pi_0^{0, f} \nabla v \right)_f + S^f \left(u - \Pi_1^{\nabla, f} u, v - \Pi_1^{\nabla, f} v \right), \quad (4.11)$$

where S^f must be chosen such that

$$\exists \alpha, \beta > 0: \forall u \in \mathcal{V}_\delta^f, \quad \alpha \left(\underline{K}_i \nabla u, \nabla u \right)_f \leq a_\delta^f(u, u) \leq \beta \left(\underline{K}_i \nabla u, \nabla u \right)_f. \quad (4.12)$$

As done for the stabilization form for polyhedra, we denote by $\text{dof}_i^f(\cdot)$ the dof-operator on \mathcal{V}_δ^f (the value at the i -th vertex of f) and choose

$$\forall u, v \in \mathcal{V}_\delta^f, \quad S^f(u, v) = \left\| \underline{K}_i \right\|_{L^\infty(f)} \sum_{i=1}^{\#\mathcal{V}_\delta^f} \text{dof}_i^f(u) \text{dof}_i^f(v). \quad (4.13)$$

To discretize terms involving time derivatives, let P denote a generic polytope being either a polyhedron in $\mathcal{T}_\mathcal{D}$ or a face lying on a fracture. We formally define the bilinear form $m_\delta^P : \mathcal{V}_\delta^P \times \mathcal{V}_\delta^P \rightarrow \mathbb{R}$ such that

$$\forall u, v \in \mathcal{V}_\delta^P, \quad m_\delta^P(u, v) = \left(\Pi_0^{0,P} u, \Pi_0^{0,P} v \right)_P + \varrho_P^d S^P \left(u - \Pi_1^{\nabla, P} u, v - \Pi_1^{\nabla, P} v \right), \quad (4.14)$$

where d is the spatial dimension of the polytope (can be either 2 for polygons, or 3 for polyhedra). By standard scaling arguments, since S^P has to satisfy either (4.9) or (4.12), we have

$$\exists \alpha, \beta > 0: \forall u \in \mathcal{V}_\delta^P, \quad \alpha(u, u)_P \leq m_\delta^P(u, u) \leq \beta(u, u)_P. \quad (4.15)$$

To introduce the discrete bilinear forms we define

$$\mathcal{V}_\delta = \{v \in H^1(\mathcal{D}) : v \in \mathcal{V}_\delta^c \quad \forall c \in \mathcal{T}_\mathcal{D}, \text{tr}_{\Gamma_D} v = 0\}. \quad (4.16)$$

The global discrete bilinear forms on \mathcal{D} , $\forall u, v \in \mathcal{V}_\delta$, can be defined as:

$$a_\delta^\mathcal{D}(u, v) = \sum_{c \in \mathcal{T}_\mathcal{D}} a_\delta^c(u, v), \quad (4.17)$$

$$m_\delta^\mathcal{D}(u, v) = \sum_{c \in \mathcal{T}_\mathcal{D}} m_\delta^c(u, v_i). \quad (4.18)$$

Similarly, for each fracture F_i , we set, $\forall u, v \in \mathcal{V}_\delta$,

$$a_\delta^{F_i}(u_i, v_i) = \sum_{f \in \mathcal{T}_{F_i}} a_\delta^f(u_i, v_i), \quad (4.19)$$

$$m_\delta^{F_i}(u_i, v_i) = \sum_{f \in \mathcal{T}_{F_i}} m_\delta^f(u_i, v_i). \quad (4.20)$$

Finally,

$$a_\delta(u, v) = a_\delta^\mathcal{D}(u, v) + \sum_{i=1}^{N_F} a_\delta^{F_i}(u_i, v_i), \quad (4.21)$$

$$m_\delta(u, v) = m_\delta^\mathcal{D}(u, v) + \sum_{i=1}^{N_F} m_\delta^{F_i}(u_i, v_i). \quad (4.22)$$

The semi-discrete formulation of (2.9) thus reads as follows: find $h \in \mathcal{V}_\delta$ such that, for all $v \in \mathcal{V}_\delta$,

$$\frac{d}{dt} m_\delta(h, v) + a_\delta(h, v) = \sum_{c \in \mathcal{T}_\mathcal{D}} \left(s, \Pi_0^{0,c} v \right)_c. \quad (4.23)$$

The above problem is well-posed since the discrete bilinear forms we defined are equivalent to the ones used in (2.9) by (4.9), (4.12) and (4.15). Optimal error convergence rates can be proved using standard arguments for virtual element methods.⁷

4.1. Continuity at the interfaces

Problem (4.23) is given by the sum of terms written on domains of different geometrical sizes, the 3D matrix and the 2D fractures, and implicitly includes the imposition of the continuity conditions at the interfaces. The possibility of enforcing continuity conditions at the 1D fracture-fracture interfaces and at the 2D matrix-fracture interfaces in an easy way is one of the key features of the proposed application of the VEM. Indeed, as shown in Figure 4, here unique degrees of freedom are used across the various domains, thus avoiding the use of Lagrange multipliers to obtain the desired matching. This, in turn, result in a symmetric positive definite system to be solved at each time-step in unstationary simulations.

5. Numerical results

In this section some numerical tests are presented on networks of increasing complexity: the first three tests take into account stationary problems, whereas the last one deals with a time-dependent simulation. In all simulations the linear systems are solved using the Cholesky factorization of the Eigen C++ library.³⁷ For time-dependent simulations a time-step of 0.001 is used with the Implicit Euler scheme.

5.1. Problem 1 - simple DFM with known solution

The first numerical test deals with the computation of the steady state distribution of the hydraulic head in a cubic domain $\mathcal{D} = [0, 1]^3$ crossed by a planar fracture, as shown in Figure 5. Dirichlet boundary conditions are set on the whole boundary and a forcing term is set such that the exact solution for this problem is $H = \frac{1}{4}(x^2 + y^2) - \frac{1}{2}\underline{\underline{K}}_F|z|$, with $\underline{\underline{K}}_F$ the hydraulic transmissivity of the unique fracture F_1 set to $\underline{\underline{K}}_F = 1000$, whereas the permeability of the block is set to $\underline{\underline{K}}_{\mathcal{D}} = 1$. The solution computed with the proposed method on a mesh of cubic cells with edge equal to 0.05 is shown in Figure 6. The L^2 and H^1 norms of the error on the whole domain are computed on four different meshes, with the number of degrees of freedom ranging between 576 and 8400. Convergence curves of the errors against the total number of degrees of freedom N_{Dofs} are reported in Figure 7 along with the expected optimal rates, equal to $\frac{2}{3}$ for the L^2 norm and $\frac{1}{3}$ for the H^1 norm; these optimal rates can be achieved despite the low regularity of the exact solution thanks to the conformity of the mesh to the irregularity interface. Indeed, if we define

$$V^2(\mathcal{D}) = \left\{ v \in V(\mathcal{D}) : v \in H^2(\hat{c}) \forall c \in \mathcal{T}_{\mathcal{D}}, v_i \in H^2(\hat{f}) \forall i \in \{1, \dots, N_F\}, f \in \mathcal{T}_{F_i} \right\},$$

14 *Berrone, Borio, D'Auria, Scialò, Vicini*

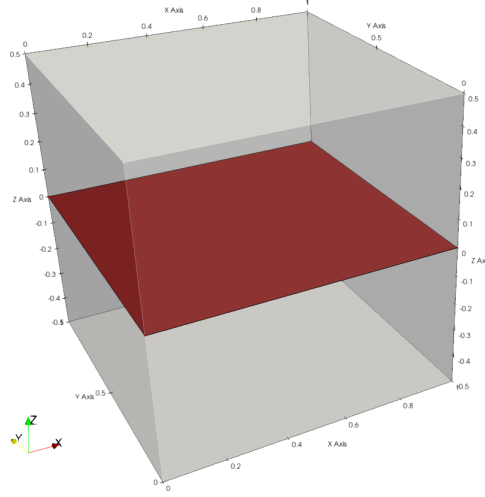


Fig. 5: Problem 1: domain description: with \mathcal{D} (white, transparent) and Ω (red)

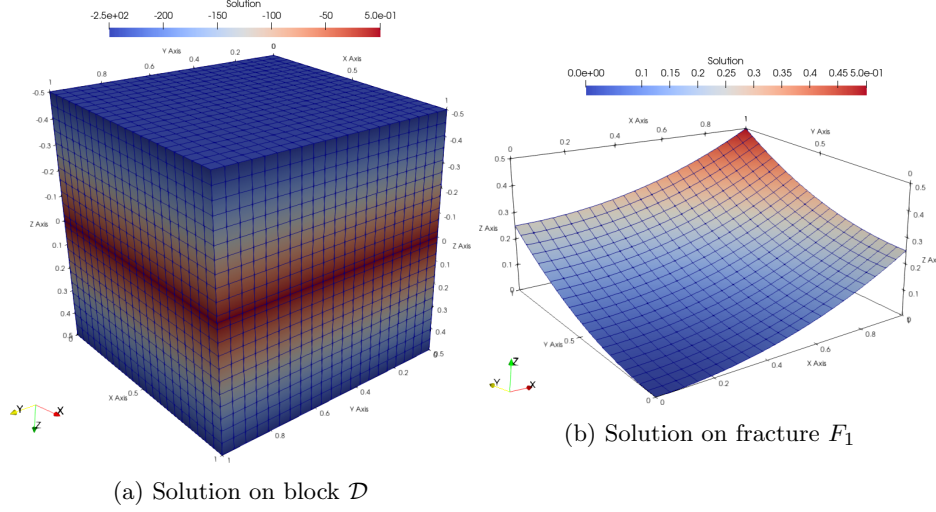


Fig. 6: Problem 1: Example mesh and solution with the VEM based approach

and

$$\rho_{\mathcal{D}} = \max_{c \in \mathcal{T}_{\mathcal{D}}} \rho_c, \quad \rho_{F_i} = \max_{f \in \mathcal{T}_{F_i}} \rho_f \quad \forall i \in \{1, \dots, N_F\},$$

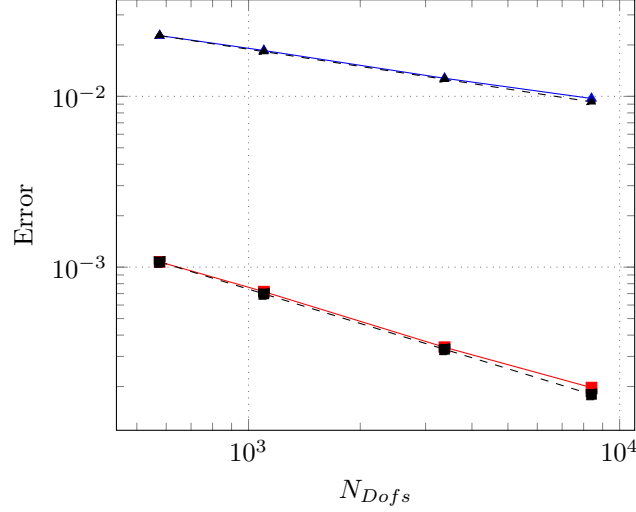


Fig. 7: Problem 1: L^2 and H^1 error convergence plots. Legend: \blacksquare L^2 norm, \blacktriangle H^1 norm, $- \blacksquare -$ L^2 norm slope $\frac{2}{3}$, $- \blacktriangle -$ H^1 norm slope $\frac{1}{3}$

and, finally,

$$\begin{aligned} |||v||| &= \sqrt{a(v, v)}, \\ \|H\|_{H^2(\tilde{\mathcal{D}})} &= \sqrt{\sum_{c \in \mathcal{T}_{\mathcal{D}}} \|H\|_{H^2(\tilde{c})}^2}, \\ \|H_i\|_{H^2(\tilde{F}_i)} &= \sqrt{\sum_{f \in \mathcal{T}_{F_i}} \|H_i\|_{H^2(f)}^2}, \end{aligned}$$

then, the following result can be proved following Ref. 7 as reported in Appendix A.

Theorem 5.1. *Assume that the solution of (2.9) in its stationary form satisfies $H \in V^2(\mathcal{D})$ and let h be the solution of (4.23) under stationary conditions. Then, there exists a constant $C > 0$ independent of the mesh size such that*

$$|||H - h||| \leq C \left(\rho_{\mathcal{D}} (\|H\|_{H^2(\tilde{\mathcal{D}})} + \|s\|_{L^2(\tilde{\mathcal{D}})}) + \sum_{i=1}^{N_F} \rho_{F_i} \|H_i\|_{H^2(\tilde{F}_i)} \right). \quad (5.1)$$

The optimal convergence rates for the L^2 error can be obtained by duality arguments.⁷ It can be seen in Figure 7 that the obtained convergence trends well adhere with the expected ones.

Remark 5.1. The assumptions on the regularity of the solution made in Theorem 5.1 can be verified observing that, since the mesh is conforming to fracture planes and to fracture intersections thanks to the meshing algorithm described in Section

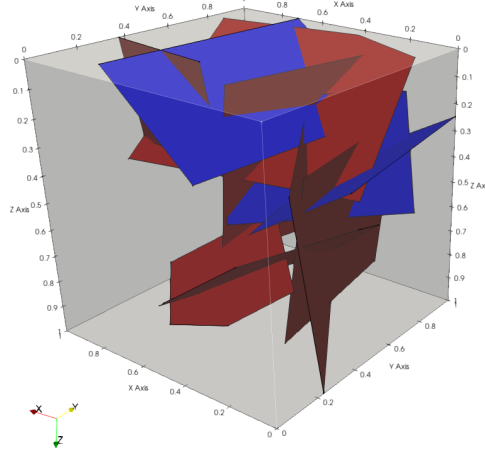


Fig. 8: Problem 2: domain description with \mathcal{D} (white, transparent) and fractures: fractures in red have $\underline{K}_F = 1$, fractures in blu have $\underline{K}_F = 10$.

Table 1: Problem 2: DFN Ω data: N_F number of fractures, N_S number of traces, N_I number of intersections between couples of traces, $\min \theta_F$ minimum angle between intersecting fractures, $\min \theta_S$ minimum angle between intersecting traces in the same fracture.

Id	N_F	N_S	N_I	$\min \theta_F$	$\min \theta_S$
DFN10	10	25	38	29.9986	7.5667

Table 2: Problem 2: mesh $\mathcal{T}_{\mathcal{D}}$ data: N_{Dofs} number of degrees of freedom, $\min \ell$, $\max \ell$, $\mathbb{E}[\ell]$ minimum, maximum, average element edge length, $\min \eta$, $\max \eta$, $\mathbb{E}[\eta]$ minimum, maximum, average element aspect ratio.

Id	Mesh	N_{Dofs}	$\min \ell$	$\max \ell$	$\mathbb{E}[\ell]$	$\min \eta$	$\max \eta$	$\mathbb{E}[\eta]$
DFN10	M1	2961	4.25e-5	1.33e-1	6.69e-2	1.73	8.06e1	5.40
DFN10	M2	45148	8.56e-7	4.62e-2	2.77e-2	1.73	1.19e2	3.16

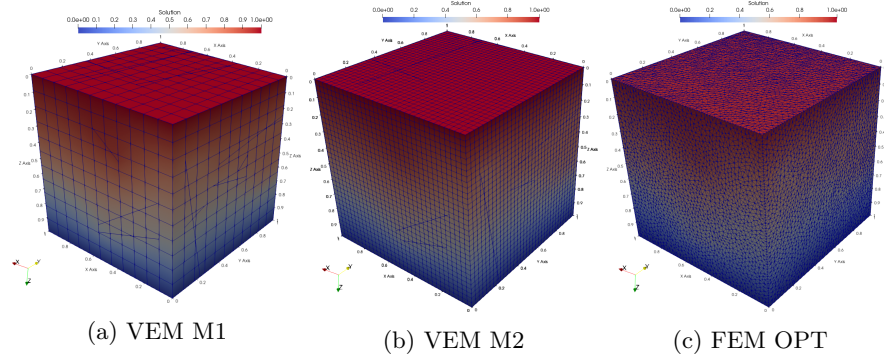
3, the solution will be locally regular in the interior of each polyhedron and each face lying on a fracture.

5.2. Problem 2 - Simple DFM problem

The second example proposes a validation of the approach on a more complex domain counting 10 fractures and 25 fracture intersections. Some additional in-

Table 3: Problem 2: condition number κ of the conforming VEM approach.

Id	Mesh	κ
DFN10	M1	9.55e4
DFN10	M2	2.66e6

Fig. 9: Problem 2: comparison of solution on \mathcal{D}

formation on the geometry of the network are reported in Table 1, where $\min \theta_F$ represents the minimum angle between two intersecting fractures, computed as the angle between the normals of the fractures, and $\min \theta_S$ is the minimum angle between couples of intersecting traces in a fracture and N_I represents the total number of intersections between couples of traces in fractures. We can see that, despite the simplicity of the network, angles as narrow as about 7.5 degrees are present, and there are 38 intersections between couples of fractures. The permeability of the porous matrix is set to one, whereas the transmissivity of three fractures, highlighted in blu in Figure 8, is set to 10; transmissivities of the remaining fractures, highlighted in red in Figure 8, is set to one. A head drop of 1 is imposed between the top and bottom faces of the domain, all other faces being instead insulated, and a null forcing term is used.

Since an analytical solution is not available for this problem, the computed steady state distribution of the hydraulic head in the network with the VEM is compared to the solution of the same problem with the optimization based approach described in Ref. 18. A mesh with about 2×10^5 tetrahedral cells and 6×10^3 triangular cells for the fractures is used for the optimization based approach (FEM OPT), counting about 4.6×10^4 total degrees of freedom. Two meshes are proposed for the VEM based approach, named M1 and M2; the latter counts about the same number of degrees of freedom of the FEM OPT, whereas the former is coarser.

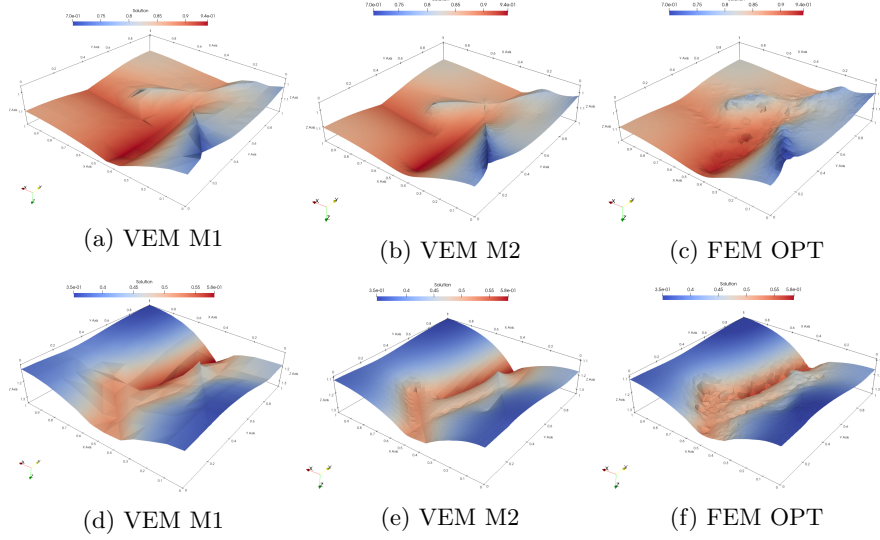


Fig. 10: Problem 2: comparison of solution obtained with the VEM and the optimization based approach on two sections of the domain with planes orthogonal to the z -axis located at $z = 0.25$ (top) and $z = 0.75$ (bottom).

Additional data on the meshes are available in Table 2: $\min \ell$, $\max \ell$, $\mathbb{E}[\ell]$ represent the minimum, the maximum and the average length of element edges in the mesh, respectively; $\min \eta$, $\max \eta$ and $\mathbb{E}[\eta]$ are, respectively, the minimum, maximum and average aspect ratio of elements in the mesh, computed as the ratio between the radius of the circumscribed and inscribed spheres for each element. We can see that elements with edges as small as about 10^{-6} are present next to edges of length five orders of magnitude larger; moreover, quite distorted elements are present. The meshes for the two approaches are reported in Figure 9 along with the obtained solution on the whole domain. The VEM can easily handle such distorted mesh, producing results in good agreement with the optimization based solution, chosen as reference for this analysis. This is further highlighted by the results reported in Figure 10, where the solution on two planes orthogonal to the z -axis located at $z = 0.25$ (top) and $z = 0.75$ (bottom) are shown, obtained with the VEM and with the optimization approach. We can see that similar trends and close values are obtained even on the coarse mesh M1, also taking into account that the solution with the optimization approach is on a mesh non conforming with the fractures. The condition number of the problem discrete matrix is reported in Table 3 for the two considered meshes. It can be seen that relatively small values are obtained, despite the presence in the meshes of small geometrical features and quite elongated elements.

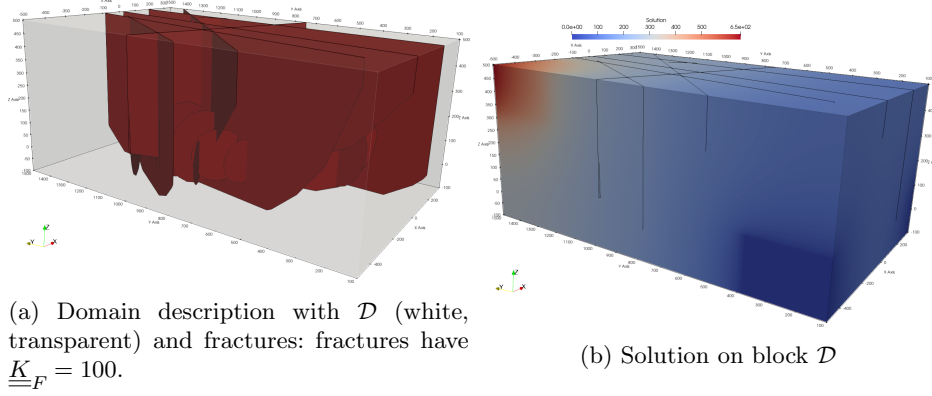


Fig. 11: Problem 3: Benchmark test

Table 4: Problem 3: mesh $\mathcal{T}_{\mathcal{D}}$ data: N_{Dof} s number of degrees of freedom, $\min \ell$, $\max \ell$, $\mathbb{E}[\ell]$ minimum, maximum, average element edge length, $\min \eta$, $\max \eta$, $\mathbb{E}[\eta]$ minimum, maximum, average element aspect ratio.

Mesh	3d cells	N_{Dof} s	$\min \ell$	$\max \ell$	$\mathbb{E}[\ell]$	$\min \eta$	$\max \eta$	$\mathbb{E}[\eta]$
M1	1.13e4	1.69e4	9.82e-3	7.81e1	3.55e1	1.95	4.35e2	5.58
M2	7.55e4	8.67e4	1.70e-3	3.90e1	2.12e1	1.88	2.25e3	5.08
M3	1.42e5	1.57e5	1.17e-6	3.26e1	1.75e1	1.96	6.25e4	9.66

5.3. Problem 3 - Benchmark Test

The third numerical example considers the benchmark test reported in Section 5.4 of Ref. 15. The domain is the box $\mathcal{D} = (-500m, 350m) \times (100m, 1500m) \times (-100m, 500m)$ as reported in Figure 11a. A uniform unitary hydraulic conductivity is prescribed for the porous matrix in \mathcal{D} . A network of 52 fractures and 106 traces is present in \mathcal{D} , represented in red in Figure 11a, obtained from a post-processing of an outcrop in the island of Algeirøyna (Norway). The network has a relatively simple structure with a minimum intersection angle between fracture normals $\min \theta_F \approx 7.4^\circ$ and presenting no intersections between traces. Fracture transmissivity is assigned to a constant value of 100. The solution of the test is obtained prescribing a zero boundary condition on $\partial\mathcal{D}_{out} = \partial\mathcal{D}_{out,0} \cup \partial\mathcal{D}_{out,1} = \{-500m\} \times (100m, 400m) \times (-100m, 100m) \cup \{350m\} \times (100m, 400m) \times (-100m, 100m)$ and a uniform unit inflow on $\partial\mathcal{D}_{in} = \partial\mathcal{D}_{in,0} \cup \partial\mathcal{D}_{in,1} = \{-500m, -200m\} \times \{1500m\} \times (300m, 500m) \cup \{-500m\} \times (1200m, 1500m) \times (300m, 500m)$, the remaining part of domain boundary being, instead, insulated. Three different VEM conforming meshes are tested, named M1, M2 and M3 respectively, whose data are reported in Table 4. Figure 11b shows the numerical solution obtained with the M3 discretization. The hydraulic head along two specified lines in the domain is measured as done

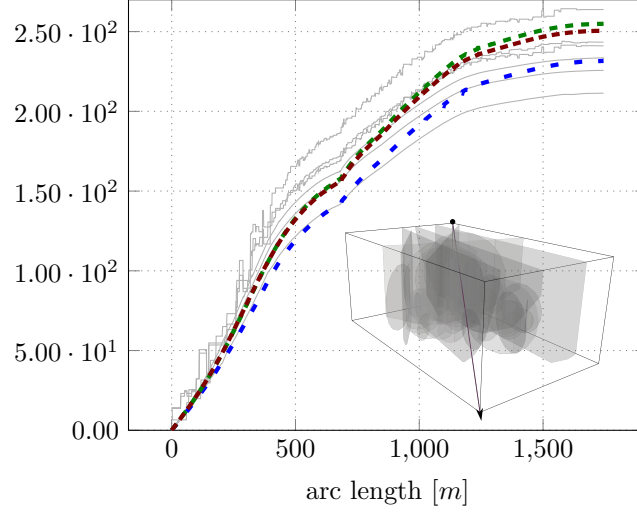
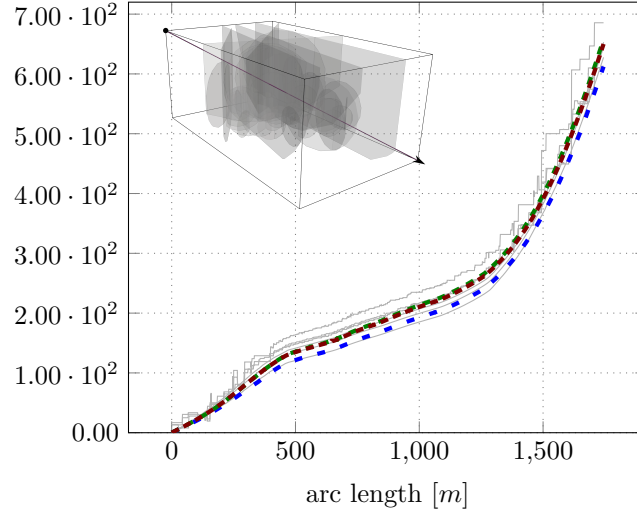
(a) Profile from outlet $\partial\mathcal{D}_{out,0}$ towards the opposite corner.(b) Profile from outlet $\partial\mathcal{D}_{out,1}$ towards $\partial\mathcal{D}_{in}$.

Fig. 12: Problem 3: Hydraulic head profiles across the domain. Legend: - - VEM M1, - - - VEM M2, - · - VEM M3, — data from benchmark work.¹⁵

in Section 5.4.2.1 of Ref. 15 and Figure 12 shows the two measured profiles. The VEM solution is compared with all the fourteen schemes proposed in the benchmark, where a fine mesh counting about 2.6×10^5 cells is used for all the schemes. It can be noticed that the VEM solution with the proposed approach is in very good agreement with the majority of the benchmark schemes, despite the meshes here

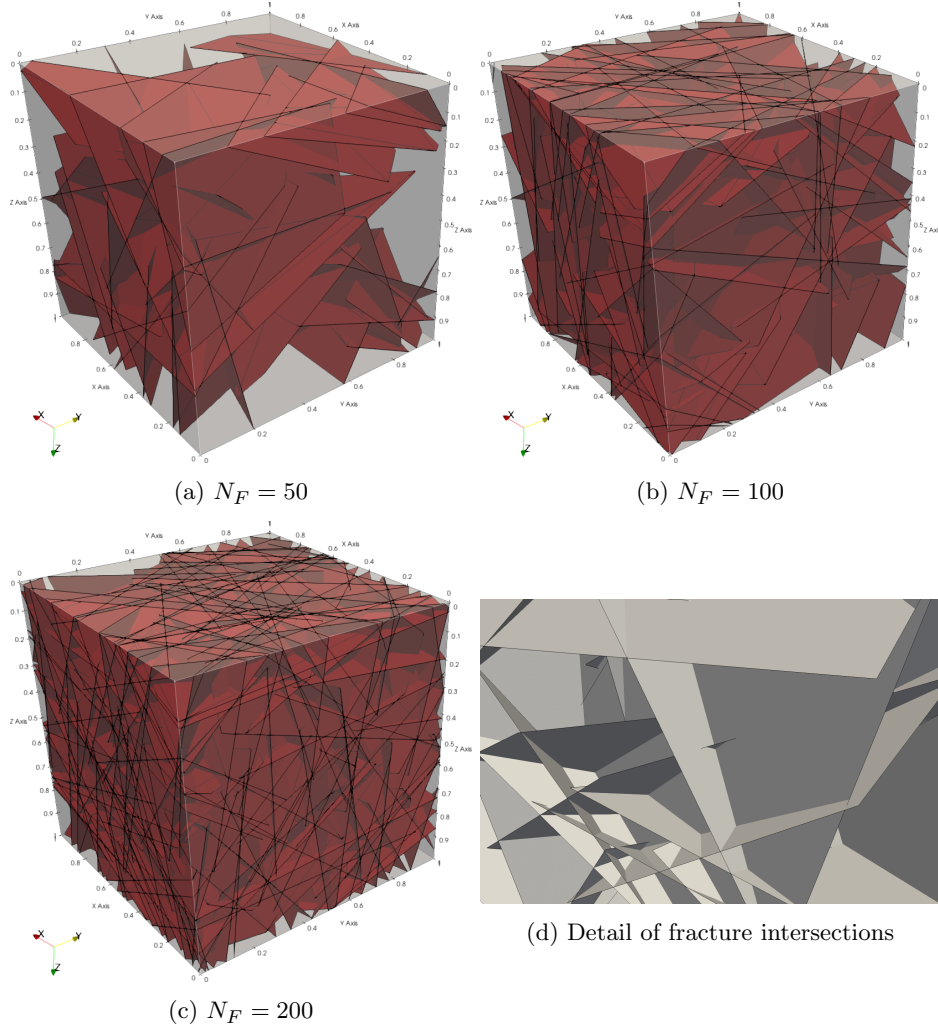


Fig. 13: Problem 4: domain description with \mathcal{D} (white) and Ω (red)

used are up to 20 times coarser.

5.4. Problem 4 - Realistic DFM problems

The fourth set of numerical tests takes into account the computation of the steady-state hydraulic head distribution in quite realistic DFM configurations, where three different and randomly generated fracture networks of increasing size are embedded in the same cubic domain, as shown in Figure 13, where the three networks are represented in red. In all cases a head drop of 1 is imposed between the top and bottom faces of the domain, all other faces being instead insulated, and a null forcing

Table 5: Problem 4: network Ω data: N_F number of fractures, N_S number of traces, N_I number of intersections between couples of traces, $\min \theta_F$ minimum angle between intersecting fractures, $\min \theta_S$ minimum angle between intersecting traces in the same fracture.

Id	N_F	N_S	N_I	$\min \theta_F$	$\min \theta_S$
DFN50	50	432	3029	10.6	2.50
DFN100	98	1587	90755	1.52	2.71e-1
DFN200	199	7351	922421	3.81	2.32e-2

Table 6: Problem 4: mesh \mathcal{T}_D data: N_{Dofs} number of degrees of freedom, $\min \ell$, $\max \ell$, $\mathbb{E}[\ell]$ minimum, maximum, average element edge length, $\min \eta$, $\max \eta$, $\mathbb{E}[\eta]$ minimum, maximum, average element aspect ratio.

Id	Mesh	N_{Dofs}	$\min \ell$	$\max \ell$	$\mathbb{E}[\ell]$	$\min \eta$	$\max \eta$	$\mathbb{E}[\eta]$
DFN50	M1	6.36e3	1.67e-5	2.74e-1	4.71e-2	1.73	2.06e2	9.56
DFN50	M2	1.32e4	1.24e-6	1.34e-1	3.74e-2	1.73	6.75e12	9.42
DFN50	M3	8.96e4	3.51e-7	4.62e-2	2.08e-2	1.73	6.75e2	6.16
DFN100	M1	2.13e4	2.60e-6	2.54e-1	3.13e-2	1.95	3.83e2	1.11e1
DFN100	M2	3.46e5	2.74e-7	1.34e-1	2.67e-2	1.73	1.70e3	1.07e1
DFN100	M3	1.55e5	2.39e-7	4.82e-2	1.68e-2	1.73	7.75e12	5.73e7
DFN200	M1	1.11e5	2.71e-7	2.07e-1	1.71e-2	1.86	1.66e3	1.13e1
DFN200	M2	1.49e5	2.25e-7	1.28e-1	1.56e-2	1.79	1.13e13	9.68e7
DFN200	M3	4.08e5	3.55e-9	5.00e-2	1.14e-2	1.72	1.49e17	4.15e11

term is used. The permeability of the matrix and the transmissivity of the fractures is set to 1. Details on the geometrical complexity of the networks are reported in Table 5: the networks count about 50, 100 and 200 fractures, forming 432, 1587 and 7351 traces, respectively. On the largest network, the minimum angle between intersecting fractures, θ_F , is less than 4 degrees, and the minimum angle between intersecting traces, θ_S , is as low as 2.3×10^{-2} , with a total number $N_I = 922421$ of trace intersections in the fractures, thus showing the severity of the configurations. This is reflected in the properties of the generated conforming meshes. Three meshes, labeled M1, M2 and M3, are considered for each problem, whose detailed data are provided in Table 6. A very large variation in terms of edge lengths ℓ can be seen and aspect ratios η for the elements can reach values as high as 10^{11} . The finest used meshes are shown in Figure 14, along with the computed solution on the whole domains, and in Figure 15, where the domains are cut to provide a view of the interior part of the mesh. Again, the proposed approach is capable of handling such meshes, producing reliable solutions, as qualitatively shown in Figure 16, where the

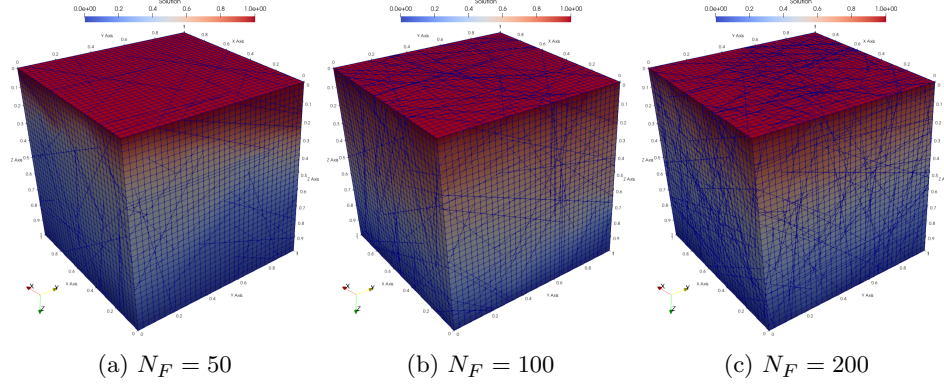


Fig. 14: Problem 4: Mesh and solutions on \mathcal{D} for the three problems: DFN50 (left), DFN100 (middle), DFN200 (right).

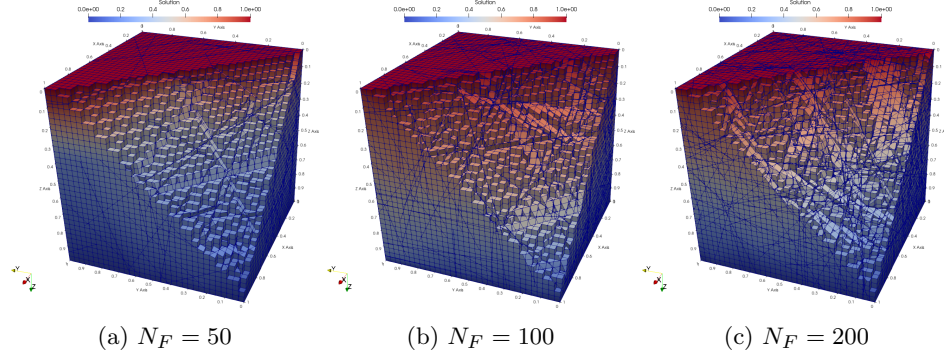


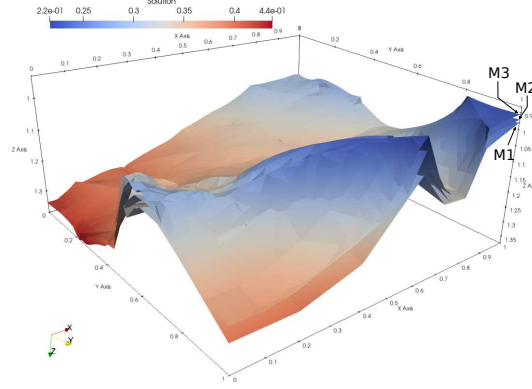
Fig. 15: Problem 4: detail of conformed mesh cut with a plane normal to $[-1, 1, 1]$ and centered in $[1, 1, 0]$. DFN50 left, DFN100 middle, DFN200 right.

solution on a plane orthogonal to the z -axis located at $z = 0.5$ is reported for the three networks and for the three considered meshes: we can see that the solution is stable at mesh refinements for all the considered cases. In Figure 16 on the z -axis we report the values of the solution multiplied by a factor ($2x$ or $3x$) in order to amplify the differences between the solutions obtained on different meshes. The reader can refer to the colorbar for the exact values.

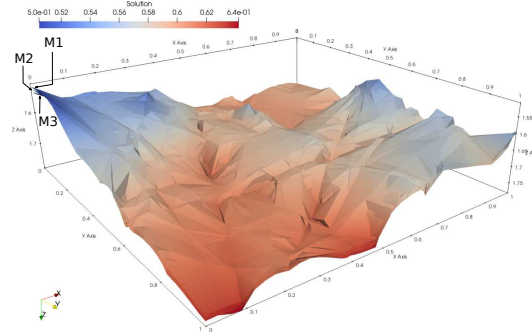
5.5. Problem 5 - Non Stationary problem

The last example considers a time-dependent simulation on the domain labeled DFN50 of the previous example (Figure 13a). A constant in time Dirichlet boundary condition equal to 1 is set on the face of the domain located at $z = 0$, whereas all

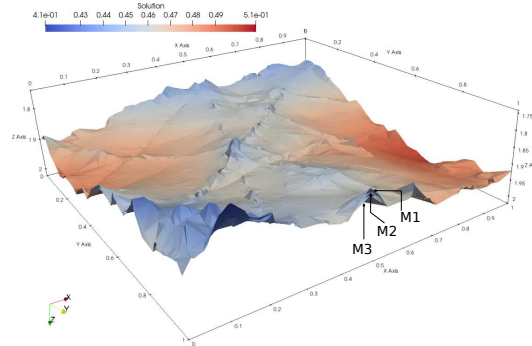
24 *Berrone, Borio, D'Auria, Scialò, Vicini*



(a) DFN50 - Rescaled 2x



(b) DFN100 - Rescaled 2x



(c) DFN200 - Rescaled 3x

Fig. 16: Problem 4: comparison of solution on a plane orthogonal to the z -axis and located at $z = 0.5$. Three meshes overlapped, M1, M2, M3.

other borders are insulated. The permeability of the matrix is set to 1, whereas fracture transmissivity is equal to 10 for all fractures. A zero initial solution is

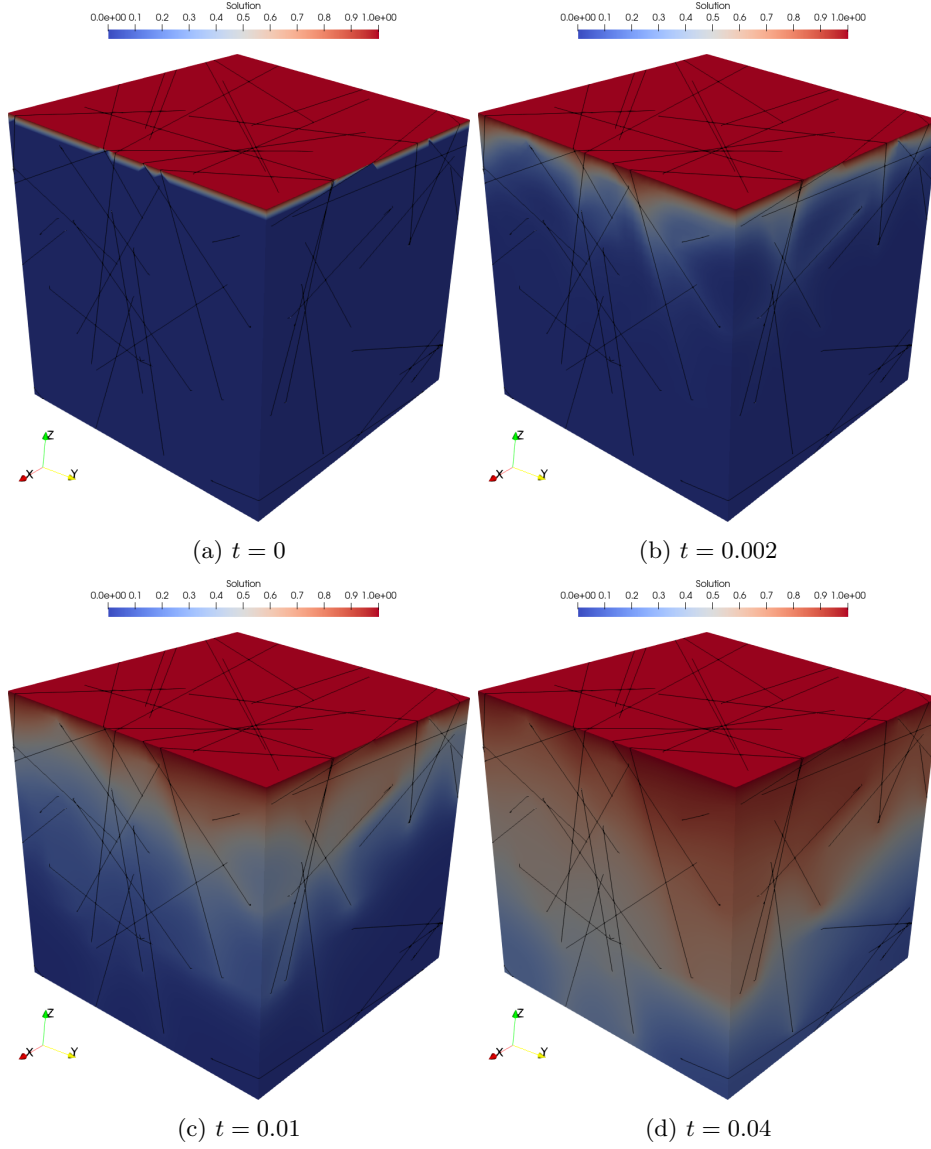


Fig. 17: Problem 5: non-stationary solution

assumed in the whole domain and a transient simulation, on the same spatial mesh as shown in Figure 14, towards the equilibrium distribution is run, using a time-step of 0.001 and setting the final time to 1. The solution at four selected time frames is reported in Figure 17, showing how the fractures represent preferential flow paths in this setting. A detail of the solution at the final simulation time is shown in Figure 18: please note that in the plot on the left the colour palette is rescaled

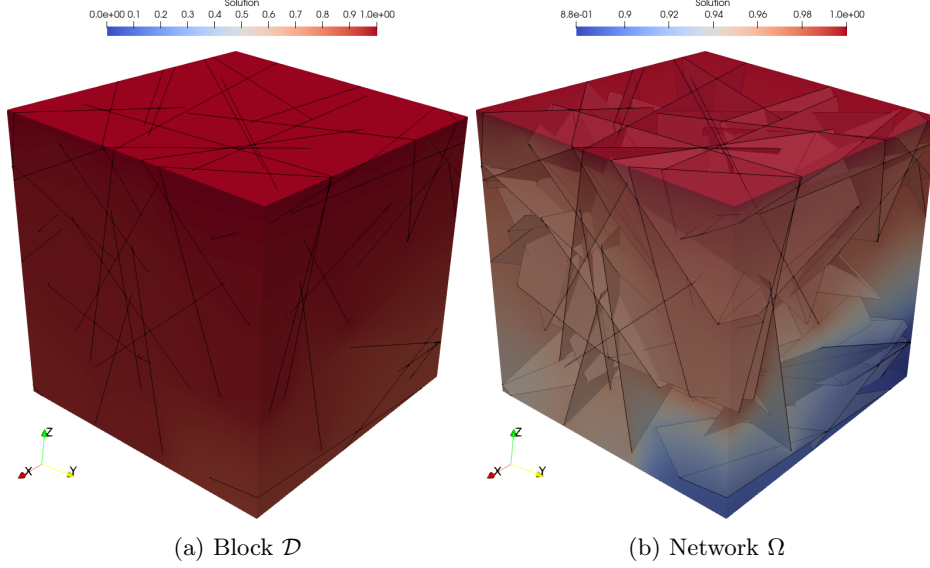


Fig. 18: Problem 5: detail of solution at $t = 1.0$

between values 0.88 and 1.0 to better highlight the variation of the solution in the domain; moreover, the domain is transparent to show the internal fracture network and its effect on the hydraulic head distribution in the network.

6. Conclusions

The proposed meshing strategy, in conjunction with a primal VEM based formulation of the hydraulic head problem in DFM, resulted in a robust and effective approach for the simulation of the flow in fractured porous media on polytopal conforming meshes. The method has been tested on a range of DFM models, starting from a simple domain with known analytic solution to more complex, realistic, configurations with challenging geometries. In all cases the meshing process was capable of producing a conforming mesh suitable for the chosen discretization method. Time dependent simulations have been effectively performed, also in complex geometries.

Appendix A. Proof of Theorem 5.1

Let $v \in V(\mathcal{D})$ be given. Then, for any face $f \subset F_i$, let

$$|||v|||_f = \sqrt{\left(\underline{K}_i \nabla_i v_i, \nabla_i v_i \right)_f}.$$

Moreover, for any cell $c \in \mathcal{T}_{\mathcal{D}}$, let

$$|||v|||_c = \sqrt{\left(\underline{K}_{\mathcal{D}} \nabla v, \nabla v \right)_c}.$$

Finally, we denote

$$|||v||| = \sqrt{a(v, v)} = \sqrt{\sum_{c \in \mathcal{T}_D} |||v|||_c^2 + \sum_{i=1}^{N_F} \sum_{f \in \mathcal{T}_{F_i}} |||v|||_f^2}.$$

We define

$$V^2(\mathcal{D}) = \left\{ v \in V(\mathcal{D}) : v \in H^2(\tilde{c}) \ \forall c \in \mathcal{T}_D, v_i \in H^2(\tilde{f}) \ \forall i \in \{1, \dots, N_F\}, f \in \mathcal{T}_{F_i} \right\},$$

and, on $V^2(\mathcal{D})$, we define the following broken norms:

$$\begin{aligned} \|H\|_{H^2(\mathcal{D})} &= \sqrt{\sum_{c \in \mathcal{T}_D} \|H\|_{H^2(\tilde{c})}^2}, \\ \|H_i\|_{H^2(\tilde{F}_i)} &= \sqrt{\sum_{f \in \mathcal{T}_{F_i}} \|H_i\|_{H^2(\tilde{f})}^2}. \end{aligned}$$

Moreover, let

$$\rho_D = \max_{c \in \mathcal{T}_D} \rho_c, \quad \rho_{F_i} = \max_{f \in \mathcal{T}_{F_i}} \rho_f \quad \forall i \in \{1, \dots, N_F\}.$$

Following Ref. 7, the proof relies on the following auxiliary result.

Lemma Appendix A.1. *Let $u \in V^2(\mathcal{D})$. Then, there exists a function $u_I \in \mathcal{V}_\delta$ such that*

$$\exists C_D > 0: \|\nabla(u - u_I)\|_{L^2(\mathcal{D})} \leq C_D \rho_D \|u\|_{H^2(\mathcal{D})}, \quad (\text{A.1})$$

$$\forall i \in \{1, \dots, N_F\}, \exists C_{F_i} > 0: \|\nabla(u_i - \text{tr}_{F_i} u_I)\|_{L^2(\tilde{F}_i)} \leq C_{F_i} \rho_{F_i} \|u_i\|_{H^2(\tilde{F}_i)}, \quad (\text{A.2})$$

where constants depend on the shape of the polytopes that discretize each domain, on \underline{K}_D and \underline{K}_i $\forall i$.

Proof. u_I can be defined as in Ref. 24 (Theorem 11), thus obtaining (A.1) from standard interpolation estimates, since $u \in H^2(\tilde{c}) \ \forall c \in \mathcal{T}_D$.

Regarding (A.2), we observe that, in the construction of u_I , the $\text{tr}_f u_I$ is defined as a VEM interpolant, $\forall f \in \mathcal{F}_{\mathcal{T}_D}$. Thus, estimate (A.2) is obtained by the interpolation estimates reported in the cited reference, since $u_i \in H^2(\tilde{f}) \ \forall i$ if $f \in \mathcal{T}_{F_i}$. \square

We are now ready to prove Theorem 5.1.

Proof. (Theorem 5.1)

Let H_I be the function described in Lemma Appendix A.1. We apply a triangle inequality and obtain:

$$|||H - h||| \leq |||H - H_I||| + |||H_I - h|||.$$

The first term can be bounded by (A.1) and (A.2):

$$|||H - H_I||| \leq C \left(\rho_{\mathcal{D}} \|H\|_{H^2(\tilde{\mathcal{D}})} + \sum_{i=1}^{N_F} \rho_{F_i} \|H_i\|_{H^2(\tilde{F}_i)} \right).$$

Setting $e_\delta = H_I - h$, exploiting the equivalence relations (4.9) and (4.12) and applying the weak formulation (2.9) and the discrete formulation (4.23) in stationary conditions, we get

$$\begin{aligned} |||e_\delta|||^2 &\leq C a_\delta(e_\delta, e_\delta) \leq C (a_\delta(H_I, e_\delta) - a_\delta(h, e_\delta) + (s, e_\delta) - a(H, e_\delta)) \\ &= C \left(\sum_{c \in \mathcal{T}_{\mathcal{D}}} \left(s, e_\delta - \Pi_0^{0,c} e_\delta \right)_c + a_\delta(H_I, e_\delta) - a(H, e_\delta) \right). \end{aligned} \quad (\text{A.3})$$

The first term in the parentheses can be bounded exploiting known results on polynomial projections.⁷ For any $c \in \mathcal{T}_{\mathcal{D}}$,

$$\left(s, e_\delta - \Pi_0^{0,c} e_\delta \right)_c \leq \|s\|_{L^2(c)} \|e_\delta - \Pi_0^{0,c} e_\delta\|_{L^2(c)} \leq C \rho_c \|s\|_{L^2(c)} |||e_\delta|||_c.$$

Regarding the other terms in (A.3), we decompose them as follows:

$$\begin{aligned} a_\delta(H_I, e_\delta) - a(H, e_\delta) &= \sum_{c \in \mathcal{T}_{\mathcal{D}}} a_\delta^c(H_I, e_\delta) - \left(\underline{K}_{\mathcal{D}} \nabla H, \nabla e_\delta \right)_c \\ &\quad + \sum_{i=1}^{N_F} \sum_{f \in \mathcal{T}_{F_i}} a_\delta^f(H_I, e_\delta) - \left(\underline{K}_i \nabla_i H, \nabla_i(\text{tr}_{F_i} e_\delta) \right). \end{aligned}$$

Terms on cells and faces lying on fractures are treated separately. $\forall c \in \mathcal{T}_{\mathcal{D}}$ we get, since $a_\delta^c(\Pi_1^{0,c} H, e_\delta) = \left(\underline{K}_{\mathcal{D}} \nabla \Pi_1^{0,c} H, \nabla e_\delta \right)_c$ and by applying (4.9), (A.1) and estimates on projectors,

$$\begin{aligned} a_\delta^c(H_I, e_\delta) - \left(\underline{K}_{\mathcal{D}} \nabla H, \nabla e_\delta \right)_c &= a_\delta^c(H_I - \Pi_1^{0,c} H, e_\delta) \\ &\quad + \left(\underline{K}_{\mathcal{D}} \left(\nabla \Pi_1^{0,c} H - \nabla H \right), \nabla e_\delta \right)_c \\ &\leq C \left(\left\| \sqrt{\underline{K}_{\mathcal{D}}} \left(\nabla H_I - \nabla \Pi_1^{0,c} H \right) \right\| \right. \\ &\quad \left. + \left\| \sqrt{\underline{K}_{\mathcal{D}}} \left(\nabla H - \nabla \Pi_1^{0,c} H \right) \right\| \right) |||e_\delta|||_c \\ &\leq C \rho_c \|H\|_{H^2(\tilde{c})} |||e_\delta|||_c. \end{aligned}$$

We can proceed similarly with the terms on faces, using $a_\delta^f(\Pi_1^{0,f} H, e_\delta) = \left(\underline{K}_i \nabla_i \Pi_1^{0,f} H, \nabla_i(\text{tr}_{F_i} e_\delta) \right)_f$, (4.12) and (A.2), obtaining

$$a_\delta^f(H_I, e_\delta) - \left(\underline{K}_i \nabla_i H, \nabla_i(\text{tr}_{F_i} e_\delta) \right) \leq C \rho_f \|H_i\|_{H^2(\tilde{f})} |||e_\delta|||_f.$$

Inequality (5.1) follows immediately from the above bounds. \square

Acknowledgment

This work is supported by the MIUR project “Dipartimenti di Eccellenza 2018-2022” (CUP E11G18000350001), PRIN project “Virtual Element Methods: Analysis and Applications” (201744KLJL-004) and by INdAM-GNCS. Computational resources were partially provided by HPC@polito.it and SmartData@polito.

References

1. B. Ahmad, A. Alsaedi, F. Brezzi, L. D. Marini and A. Russo, Equivalent projectors for virtual element methods, *Computers & Mathematics with Applications* **66** (2013) 376–391.
2. R. Ahmed, M. Edwards, S. Lamine, B. Huisman and M. Pal, Control-volume distributed multi-point flux approximation coupled with a lower-dimensional fracture model, *Journal of Computational Physics* **284** (2015) 462 – 489.
3. O. Al-Hinai, S. Srinivasan and M. F. Wheeler, Mimetic finite differences for flow in fractures from microseismic data, in *SPE Reservoir Simulation Symposium* (Society of Petroleum Engineers, 2015).
4. Angot, Philippe, Boyer, Franck and Hubert, Florence, Asymptotic and numerical modelling of flows in fractured porous media, *ESAIM: M2AN* **43** (2009) 239–275.
5. P. F. Antonietti, L. Formaggia, A. Scotti, M. Verani and N. Verzott, Mimetic finite difference approximation of flows in fractured porous media, *ESAIM: Mathematical Modelling and Numerical Analysis* **50** (2016) 809–832.
6. L. Beirão da Veiga, F. Brezzi, L. D. Marini and A. Russo, The hitchhiker’s guide to the virtual element method, *Math. Models Methods Appl. Sci* **24** (2014) 1541–1573.
7. L. Beirão da Veiga, F. Brezzi, L. D. Marini and A. Russo, Virtual element methods for general second order elliptic problems on polygonal meshes, *Mathematical Models and Methods in Applied Sciences* **26** (2015) 729–750.
8. L. Beirão da Veiga, F. Brezzi, L. D. Marini and A. Russo, Mixed virtual element methods for general second order elliptic problems on polygonal meshes, *ESAIM: Mathematical Modelling and Numerical Analysis* **50** (2016) 727–747.
9. L. Beiro da Veiga, C. Lovadina and A. Russo, Stability analysis for the virtual element method, *Mathematical Models and Methods in Applied Sciences* **27** (2017) 2557–2594.
10. M. F. Benedetto, S. Berrone and A. Borio, The Virtual Element Method for underground flow simulations in fractured media, in *Advances in Discretization Methods* (Springer International Publishing, Switzerland, 2016), volume 12 of *SEMA SIMAI Springer Series*, pp. 167–186.
11. M. F. Benedetto, S. Berrone, A. Borio, S. Pieraccini and S. Scialò, A hybrid mortar virtual element method for discrete fracture network simulations, *J. Comput. Phys.* **306** (2016) 148–166.
12. M. F. Benedetto, S. Berrone, S. Pieraccini and S. Scialò, The virtual element method for discrete fracture network simulations, *Comput. Methods Appl. Mech. Engrg.* **280** (2014) 135 – 156.
13. M. F. Benedetto, S. Berrone and S. Scialò, A globally conforming method for solving flow in discrete fracture networks using the virtual element method, *Finite Elements in Analysis and Design* **109** (2016) 23 – 36.
14. M. F. Benedetto, A. Borio, F. Kyburg, J. Mollica and S. Scialò, An arbitrary order Mixed Virtual Element formulation for coupled multi-dimensional flow problems, 2020, arXiv:2001.11309.
15. I. Berre, W. M. Boon, B. Flemisch, A. Fumagalli, D. Gläser, E. Keilegavlen, A. Scotti,

30 Berrone, Borio, D'Auria, Scialò, Vicini

- I. Stefansson, A. Tatomir, K. Brenner, S. Burbulla, P. Devloo, O. Duran, M. Favino, J. Hennicker, I.-H. Lee, K. Lipnikov, R. Masson, K. Mosthaf, M. G. C. Nestola, C.-F. Ni, K. Nikitin, P. Schädle, D. Svyatskiy, R. Yanbarisov and P. Zulian, Verification benchmarks for single-phase flow in three-dimensional fractured porous media, *Advances in Water Resources* **147** (2021) 103759.
16. S. Berrone and A. Borio, Orthogonal polynomials in badly shaped polygonal elements for the Virtual Element Method, *Finite Elements in Analysis & Design* **129** (2017) 14–31.
17. S. Berrone, A. Borio and A. D'Auria, Refinement strategies for polygonal meshes applied to adaptive vem discretization, *Finite Elements in Analysis and Design* **186** (2021) 103502.
18. S. Berrone, A. D'Auria and S. Scialò, An optimization approach for flow simulations in poro-fractured media with complex geometries, *Comput Geosci*.
19. S. Berrone, A. D'Auria and F. Vicini, Fast and robust flow simulations in discrete fracture networks with GPGPUs, *International Journal on Geomathematics* **10** (2019) 8.
20. S. Berrone, D. Grappein, S. Pieraccini and S. Scialò, A three-field based optimization formulation for flow simulations in networks of fractures on non conforming meshes, 2019, arXiv:1912.09744.
21. S. Berrone, S. Pieraccini and S. Scialò, Flow simulations in porous media with immersed intersecting fractures, *Journal of Computational Physics* **345** (2017) 768 – 791.
22. S. Berrone, S. Scialò and F. Vicini, Parallel meshing, discretization and computation of flow in massive Discrete Fracture Networks, *SIAM J. Sci. Comput.* **41** (2019) C317–C338.
23. K. Brenner, M. Groza, C. Guichard, G. Lebeau and R. Masson, Gradient discretization of hybrid dimensional Darcy flows in fractured porous media, *Numerische Mathematik* **134** (2016) 569–609.
24. A. Cangiani, E. H. Georgoulis, T. Pryer and O. J. Sutton, A posteriori error estimates for the virtual element method, 2016, available online at <http://adsabs.harvard.edu/abs/2016arXiv160305855C>.
25. C. Canuto, S. Pieraccini and D. Xiu, Uncertainty quantification of discontinuous outputs via a non-intrusive bifidelity strategy, *Journal of Computational Physics* **398** (2019) 108885.
26. F. Chave, D. Di Pietro and L. Formaggia, A hybrid high-order method for darcy flows in fractured porous media, *SIAM Journal on Scientific Computing* **40** (2018) A1063–A1094.
27. Z. Chen, G. Huan and Y. Ma, *Computational Methods for Multiphase Flows in Porous Media* (SIAM, Philadelphia, PA, USA, 2006).
28. J. Coulet, I. Faille, V. Girault, N. Guy and F. Nataf, A fully coupled scheme using virtual element method and finite volume for poroelasticity, *Computational Geosciences* **24** (2019) 381–403.
29. W. S. Dershowitz and C. Fidelibus, Derivation of equivalent pipe networks analogues for three-dimensional discrete fracture networks by the boundary element method, *Water Resource Res.* **35** (1999) 2685–2691.
30. I. Faille, A. Fumagalli, J. Jaffré and J. E. Roberts, Model reduction and discretization using hybrid finite volumes for flow in porous media containing faults, *Computational Geosciences* **20** (2016) 317–339.
31. C. Fidelibus, The 2d hydro-mechanically coupled response of a rock mass with fractures via a mixed BEM-FEM technique, *International Journal for Numerical and*

- Analytical Methods in Geomechanics* **31** (2007) 1329–1348.
32. L. Formaggia, A. Fumagalli, A. Scotti and P. Ruffo, A reduced model for Darcys problem in networks of fractures, *ESAIM: Mathematical Modelling and Numerical Analysis* **48** (2014) 1089–1116.
 33. A. Fumagalli and E. Keilegavlen, Dual virtual element method for discrete fractures networks, *SIAM Journal on Scientific Computing* **40** (2018) B228–B258.
 34. A. Fumagalli, E. Keilegavlen and S. Scialò, Conforming, non-conforming and non-matching discretization couplings in discrete fracture network simulations, *J. Comput. Phys.* **376** (2019) 694–712.
 35. A. Fumagalli and A. Scotti, A numerical method for two-phase flow in fractured porous media with non-matching grids, *Advances in Water Resources* **62** (2013) 454 – 464.
 36. Fumagalli, Alessio and Keilegavlen, Eirik, Dual virtual element methods for discrete fracture matrix models, *Oil Gas Sci. Technol. - Rev. IFP Energies nouvelles* **74** (2019) 41.
 37. G. Guennebaud, B. Jacob et al., Eigen v3, <http://eigen.tuxfamily.org>, 2010.
 38. J. D. Hyman, S. Karra, N. Makedonska, C. W. Gable, S. L. Painter and H. S. Viswanathan, dfnworks: A discrete fracture network framework for modeling sub-surface flow and transport, *Computers & Geosciences* **84** (2015) 10 – 19.
 39. L. Li and S. H. Lee, Efficient Field-Scale Simulation of Black Oil in a Naturally Fractured Reservoir Through Discrete Fracture Networks and Homogenized Media, *SPE Reservoir Evaluation & Engineering* **11**.
 40. V. Martin, J. Jaffr and J. Roberts, Modeling fractures and barriers as interfaces for flow in porous media, *SIAM Journal on Scientific Computing* **26** (2005) 1667–1691.
 41. A. Moinfar, A. Varavei, K. Sepehrnoori and R. Johns, Development of an Efficient Embedded Discrete Fracture Model for 3D Compositional Reservoir Simulation in Fractured Reservoirs, *SPE Journal* **19**.
 42. S. P. Neuman, Trends, prospects and challenges in quantifying flow and transport through fractured rocks, *Hydrogeol. J.* **13** (2005) 124–147.
 43. T. D. Ngo, A. Fournon and B. Noetinger, Modeling of transport processes through large-scale discrete fracture networks using conforming meshes and open-source software, *Journal of Hydrology* **554** (2017) 66 – 79.
 44. B. Noetinger, A quasi steady state method for solving transient Darcy flow in complex 3D fractured networks accounting for matrix to fracture flow, *J. Comput. Phys.* **283** (2015) 205–223.
 45. B. Noetinger and N. Jarrige, A quasi steady state method for solving transient Darcy flow in complex 3D fractured networks, *J. Comput. Phys.* **231** (2012) 23–38.
 46. A. W. Nordqvist, Y. W. Tsang, C. F. Tsang, B. Dverstop and J. Andersson, A variable aperture fracture network model for flow and transport in fractured rocks, *Water Resource Res.* **28** (1992) 1703–1713.
 47. S. Pieraccini, Uncertainty quantification analysis in discrete fracture network flow simulations, *International Journal on Geomathematics* **11**.
 48. D. Qi and T. Hesketh, An analysis of upscaling techniques for reservoir simulation, *Petroleum Science and Technology* **23** (2005) 827–842.
 49. T. Sandve, I. Berre and J. Nordbotten, An efficient multi-point flux approximation method for discrete fracturematrix simulations, *Journal of Computational Physics* **231** (2012) 3784 – 3800.
 50. I. Stefansson, I. Berre and E. Keilegavlen, Finite-volume discretisations for flow in fractured porous media, *Transport in Porous Media* **124**.